Application of NLR's Calculation Methods to Transonic Flow About Oscillating Wings

M. H. L. Hounjet,* J. T. van der Kolk,† and J. J. Meijer‡
National Aerospace Laboratory (NLR), Amsterdam, the Netherlands

Unsteady and quasisteady aerodynamic loads in the transonic flow domain have been obtained from the numerical simulation methods of the National Aerospace Laboratory (NLR) for transonic potential flow. The unsteady results have been obtained with the time-linearized finite volume method FTRAN3, embedding a so-called field panel method which accounts for proper radiation of signals toward infinity. The mean steady flowfields and the quasisteady results have been obtained from the application of XFLO22—the NLR system for the simulation of steady transonic flow about wings and wing bodies. The calculations have been performed for several wing planforms and the results are compared with experimental data. A correlation is made between the quasisteady results of XFLO22 and FTRAN3. Flutter applications to a transonic transport wing model and a fighter configuration have been made.

Introduction

COMPUTATIONAL methods for unsteady airloads on oscillating wings in transonic flow are important 1) to assist in flutter certification calculations for aircraft in a military as well as a civil industrial environment, and 2) to support airloads and pressure measurements on oscillating wings in the wind tunnel.

During the last decade several computational methods were presented, of which the USTF3 code of Isogai[1] seems to be the most developed. Recently, also at the National Aerospace Laboratory (NLR) a three-dimensional code has been developed with the following characteristics:

1) Any steady solution can be input for an unsteady calculation (transonic small perturbation (TSP), full potential (FP), TSP + viscous effects, FP + viscous effects, and experimental data).

2) Low computational cost (CPU run time about 1 min on a CDC 7600).

3) No severe limitations to frequency range, Mach range, or planform.

4) "Exact" fulfillment of radiation conditions, i.e., no erroneous energy sinks or sources, which is an important feature for flutter investigations (full aerodynamic energy balance).

5) Easy grid generation due to finite volume formulation and relatively small extension of the grid system.

The restriction to flows with small displacements of the shocks seems to be only a minor problem in flutter analysis where usually only infinitely small wing motions are considered. In Ref. 2, calculations with FTRAN3 were discussed in which mainly a coarse idealization of the mean steady flowfield was used, approximated from measured data. The purpose of the present paper is to demonstrate the potentialities of FTRAN3 by showing results of calculations for several planforms in transonic flow where the mean steady flowfields have been determined by application of the XFLO22 code. An extensive comparison with experimental data as well as a quasisteady comparison between XFL022 and FTRAN3 results are presented. Flutter applications are presented for a transonic transport wing model and a fighter configuration.

Presented as Paper 84-1564 at the AIAA 17th Fluid Dynamics, Plasma Dynamics and Lasers Conference, Snowmass, CO, June 25-27, 1984; received Aug. 8, 1984; revision received June 6, 1985.

*Research Engineer, Department of Aeroelasticity.
†Senior Research Engineer, Department of Theoretical Aerodynamics.
‡Senior Research Engineer, Department of Aeroelasticity.

Methods

FTRAN3

Since its introduction in Ref. 2, FTRAN3 has not changed significantly. The code still solves the time-linearized full potential equation with small-disturbance boundary conditions and pressure representations. A *new line relaxation* method has been developed and implemented that is different from other line relaxation methods by not restricting the corrections of the velocity potential to the current line itself but to continue them a few grid points in a direction perpendicular to the relaxed line with a distribution rule satisfying a one-dimensional equation in that particular direction. At present, the one-dimensional subsonic equation is applied as a generator for the distribution rules. Experience with this new scheme shows that it increases the smoothing performance, especially for large-aspect-ratio cells, and is less sensitive for increasing frequency.

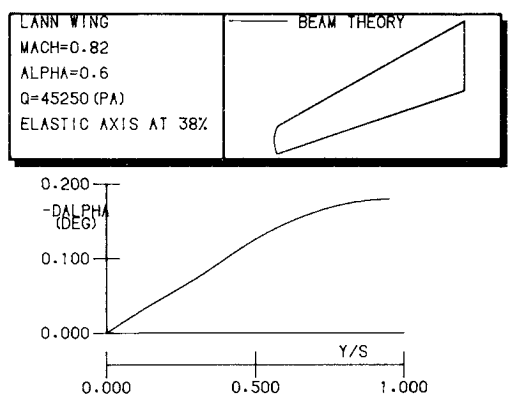

Fig. 1 Calculated model deformation of the LANN wing.

XFLO22

At NLR, XFL022 serves as a production code for calculating steady transonic full potential flow around wing-body configurations.[3] The original XFLO22 code of Jameson[11] was extended with an automated Richardson extrapolation procedure, improving the computational time by about a factor of 2. Grid sizes as well as grid distribution functions were adjusted to give better resolution near the wing root and/or tip. Body effects may be simulated by specifying boundary conditions in a cross-wind plane near the wing root using cross-wind velocities obtained from the NLR panel method.[4] For the present applications, however, no cross-wind effects are taken into account, except for the fighter configuration.

Interfacing XFLO22/FTRAN3

The interpolation of the XFLO22 potential flowfield into the mesh system utilized by FTRAN3 is accomplished as follows:

1) In each XFLO22 chordwise section, a rectangular grid system is generated whose upper and lower horizontal lines start at the top and bottom of the profile, respectively.

2) In each section the XFLO22 potentials are bilinearly interpolated to the rectangular grid.

3) The horizontal upper and lower grid lines are shifted down and up, respectively, toward the mean position of the airfoil without changing the interpolated potentials.

4) The results of the shifted mesh system are trilinearly interpolated to the mesh system of FTRAN3.

Flutter Methods

The flutter calculation methods applied herein are the well-known *k* or *V-g* method and the *pk* method.[5]

Applications

The applicability of FTRAN3 and XFLO22 to unsteady, quasisteady, and/or steady potential flow problems is demonstrated for the following wings: 1) LANN transport-type wing,[6] 2) transonic transport-type wing,[7] and 3) fighter-type configuration.

The LANN Transport-type Wing

The LANN application has been selected in order to contribute to the AGARD data base for oscillating wings in transonic flow. The LANN wing model, which was wind tunnel tested at NLR,[6] is characterized by supercritical wing sections, moderate sweep, and a high aspect ratio. No body was included. The forced harmonic unsteady motion of the "rigid" model was pitching. Due to the fact that the frequency of the first bending mode was located in the middle of the unsteady test program, the effective displacement modes have a nonzero bending component.

Steady Flowfield

The LANN wing geometry is taken from Ref. 6.§ The static wing deformation was calculated using experimental data for $Ma=0.82$, $\alpha=0.588$ deg, and $q=45{,}250$ Pa, as shown in Fig. 1. In order to match the experimental condition $\alpha=0.588$ deg, steady flowfield calculations for the deformed LANN wing were performed with the XFLO22 system, for $Ma=0.82$, and four angles of attack $\alpha=0.35$, 0.60, 0.85, and 1.5 deg. The XFLO22 calculations were performed on three successive grids using Richardson extrapolation up to engineering accuracy and with 100 extra interations on the finest ($16\times32\times28$) grid. At the wing trailing edge the flow is directed along the wing's lower surface. The CPU run time for one XFLO22 run was about 1 h.

§Due to the rather poor quality of the measured geometrical data, some smoothing was performed on the LANN wing section coordinates.

As compared with the experimental data for $\alpha=0.588$ deg, the calculation for $\alpha=0.85$ deg has the best agreement. A comparison of pressure distributions is shown in Fig. 2. Good agreement is shown for these conditions for both shock positions and peak suction levels at the leading edge.

Unsteady Flowfield

An extensive comparison has been carried out between the results of 1) FTRAN3 calculations, 2) quasisteady XFLO22 calculations, and 3) experiment.

FTRAN3 Calculations

Using interpolated data from the steady XFLO22 calculation at $Ma=0.82$ and $\alpha=0.85$ deg, the FTRAN3 code has been applied for a sequence of eight frequencies on a grid of $15\times28\times26$ (spanwise × streamwise × normalwise) points. For each frequency, convergence was obtained within 10 iterations for an accuracy of about three digits. The elasped CPU time totaled approximately 28 min on the CDC 170-855 (about 14 min on the Cyber 7600). The displacement modes were approximated from the measurements by the polynominal distributions

$$h(k)=\sum_{i=0}^{1}\sum_{j=0}^{3}C_{ij}^{(k)}x^iy^j$$

where C is complex.

Quasisteady XFLO22 Calculations

The quasisteady XFLO22 results were obtained using four-point Lagrange differentiation at $\alpha=0.85$ deg. The abscissas were $\alpha=0.35$, 0.60, 0.85, and 1.5 deg, respectively. Due to the large intervals the quasisteady results probably have been maleffected by nonlinear effects. However, selecting smaller intervals would lead to serious repercussions with respect to truncation errors and the number of necessary iterations (computer cost).

Experiment

The experimental results were obtained from Ref. 6. Caution should be exercised regarding the integrated experimental data affected by an insufficient number of operative pressure holes in important flow regions. Perhaps this could explain the large nonlinearity in the measured integrated loads presented subsequently. The quasisteady results were obtained by central differences.

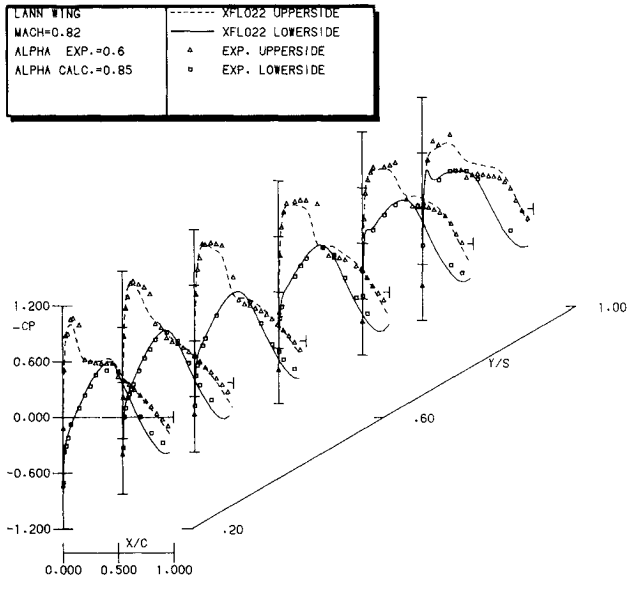

Fig. 2 Comparison of experimental and calculated distributions of steady pressure coefficients on the LANN wing.

Comparison of First-Harmonic Overall Loads

Figure 3 shows a comparison for overall wing loads vs frequency (definitions in Ref. 6). The trends are predicted correctly and the effect of the first bending model resonance frequency at $k=0.2$ is clearly demonstrated. The correlation between the calculations at $k=0$ is reasonable. The experimental upper-side loads (Fig. 3b) are strongly influenced by amplitude effects (integration resolution effects). The comparison at the lower side of the wing for the real part of the normal load is disappointing (Fig. 3c), since it was expected that a good agreement would exist between calculations and experiment in subsonic flow.

Comparison of First-Harmonic Sectional Loads

A comparison of the sectional normal load coefficients at selected frequencies is illustrated in Figs. 4 and 5; also, the trends correlate well. The effect of amplitude in the experimental data is more significant for the real part than for the imaginary part. The underprediction by the calculated imaginary part is curious since it is expected that the introduction of viscous effects to the inviscid calculations would amplify the difference.[8] The level of the real part decreases and the imaginary part becomes more negative with increasing frequency.

Surprisingly, the overprediction of the real part of the lift is more significant for the lower side than for the upper side (Fig. 5). The loading at the upper side is concentrated more inboard than at the lower side.

Comparison of Quasisteady Pressures

Figure 6 shows a comparison of calculated and measured quasisteady upper and lower-side pressures at selected stations along the span.

Upper Side

At $Y/S=0.2$, upper side, two shock peaks are shown. At the more outboard sections one shock peak remains, of which the strength decreases toward the tip.

The agreement between the calculations and the measured data is reasonable. The effect of amplitude in the experimental data is significant from the leading edge to the shock and beyond. The comparisons between the calculations show that an acceptable agreement exists outside of the shock trajectories. The differences at the leading edge are due to the small-disturbance boundary conditions and the pressure representation, and partly due to the interpolation procedure. Near the trailing edge, the disagreement is probably a result of the grid system employed in XFLO22. A comparison of the shock peaks is irrelevant here because in a time-linearized method based on a steady flowfield only the integrated shock load, which is captured in FTRAN3 with a few mesh points, has significance. (Should the calculations be based on a mean steady flowfield, the shock peaks would have significance, indeed.)

Lower Side

Except for an obvious nonlinear effect in the XFLO22 results at the midchord, a good agreement is shown at the lower side. The absence of pressure information at the midchord of the section at $Y/S=0.475$ explains, in part, the low level of the experimental loads at the lower side. At the leading-edge region the agreement between XFLO22 and the experiment is excellent. A satisfactory agreement is also obtained between FTRAN3 and the experiment in that region. At the trailing-edge region the differences between the results of XFLO22 and FTRAN3 probably are due to the XFLO22 grid system.

Comparison of First-Harmonic Pressures

Figure 7 shows a comparison of calculated and measured real parts of the first-harmonic pressures at the upper and

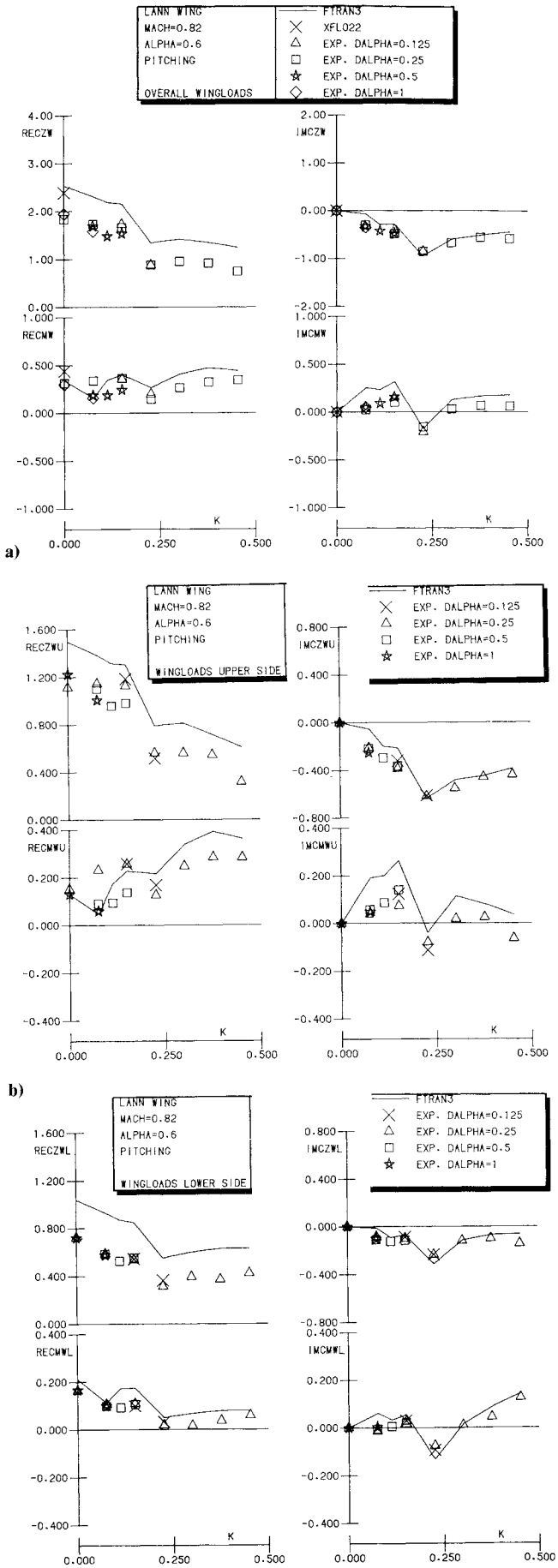

Fig. 3 Comparison of experimental and calculated unsteady lift and moment coefficients on the LANN wing.

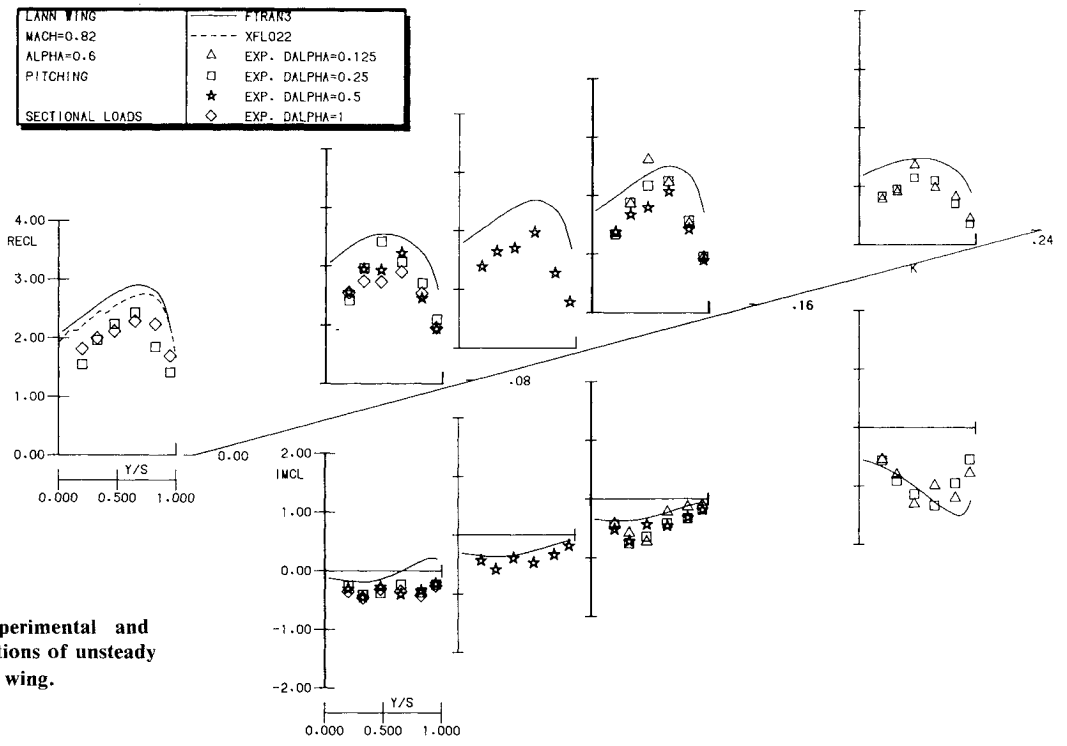

Fig. 4 Comparison of experimental and calculated spanwise distributions of unsteady lift coefficients on the LANN wing.

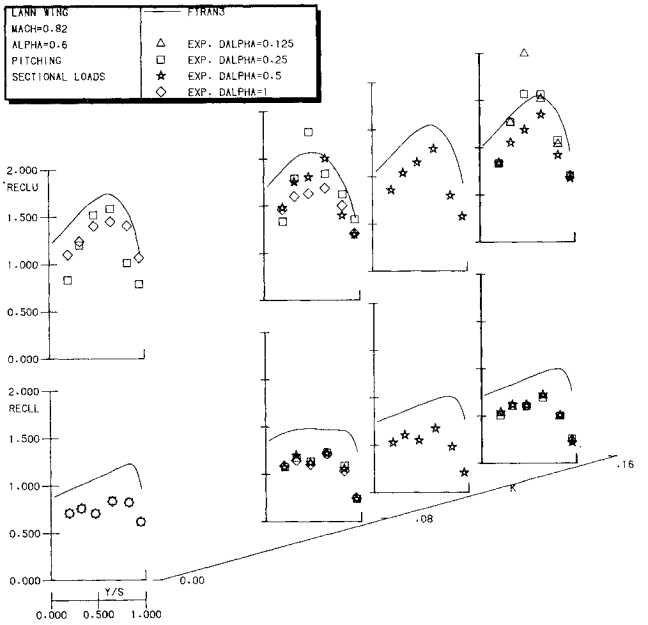

Fig. 5 Comparison of experimental and calculated spanwise distributions of the real part of unsteady lift coefficients on the LANN wing.

lower sides for $k=0.152$. The agreement between theory and experiment is reasonable. At the lower side the incomplete pressure information should explain most of the low level of the measured real experimental loads. Figure 8 shows a comparison of calculated and measured imaginary parts of the first-harmonic pressures at the upper and lower sides for $k=0.453$. Again, the agreement between theory and experiment is reasonable.

Effect of Frequency

The effect of frequency on the pressure distribution is illustrated in Fig. 9, where the first-harmonic upper- and lower-side pressures at $Y/S=0.475$ are plotted vs frequency. The agreement between theory and experiment is reasonable over the entire frequency range. The level of the real pressures decreases and the level of the imaginary pressures increases with increasing frequency. The sign of the measured imaginary part of the leading-edge peak at the lower side for the lower frequencies is a bit puzzling (stagnation-point effect?).

Supercritical Transport Wing Model

The applicability of FTRAN3 in flutter analyses is presented for a large-aspect-ratio supercritical transport wing that was tested extensively in the NLR wind tunnel[7] and has also been used at NLR for the verification of other transonic calculation methods.[9] Because flutter boundaries dominated by viscous effects are more likely to be predicted conservatively with inviscid methods, the emphasis herein is to investigate if a conservative prediction of the flutter boundaries in transonic attached flow situations can be obtained by using the three-dimensional inviscid full potential airloads of FTRAN3. Two experimental conditions were selected for a comparison: 1) $Ma=0.75$, $\alpha=-0.64$ deg, and 2) $Ma=0.70$, $\alpha=1.78$ deg.

Steady Flowfield

Steady flowfields were calculated for $Ma=0.75$ and $\alpha=0$, -1, and -2 deg, and $Ma=0.7$ and $\alpha=1$, 2, and 3 deg using the XFLO22 code. Results, in terms of pressure distributions, are compared in Figs. 10 and 11 with experimental data of earlier steady pressure model tests for the two conditions selected. The comparison shows good agreement for both peak suction levels and shock positions. The calculations were performed in the same manner as indicated for the LANN wing.

Unsteady Flowfield

The unsteady FTRAN3 calculations have been performed for four frequencies, two vibration modes, and the flow conditions $\alpha=-1$ deg, $Ma=0.75$ and $\alpha=2$ deg, $Ma=0.7$. Figure 12 shows the two vibration modes that control the flutter characteristics. The modes—fundamental wing bending and torsion—were approximated from the measured data by a polynominal distribution such as was used for the LANN wing

application. In order to demonstrate the effect of the grid, the calculations have been performed on two grids: a coarse grid (60 points on each wing upper and lower surface, $9 \times 16 \times 14$ field points) and a fine grid (240 points on each wing surface, $15 \times 28 \times 26$ field points). The total CPU time for this exercise with the unsteady flowfield was about 1 h. An example of the unsteady calculations is depicted in Fig. 13, which shows a perspective view of calculated first-harmonic pressures at the upper and lower sides of the wing for the torsion mode and second flow condition. The lower side clearly shows a subsonic distribution, while the upper side shows dominating contribution of the shock waves. At the tip and root the distribution at the upper side falls downward rapidly into a subsonic character.

Flutter Boundaries

The flutter calculations were performed with the *pk* method in a version for constant Mach number with variable wind tunnel stagnation pressure. The results are depicted in Fig. 14, where a comparison is made between doublet-lattice, experimental, and FTRAN3 flutter boundaries. During the flutter test, the angles of attack depended on Mach number and stagnation pressure. Because the available unsteady airloads were calculated using FTRAN3, comparisons could be made only for $Ma = 0.75$, $\alpha_{exp} = -0.64$ deg and $Ma = 0.7$, $\alpha_{exp} = 1.78$ deg. Compared with the doublet-lattice results, the FTRAN3 airloads have a strong decreasing effect on the calculated flutter boundaries. The first FTRAN3 application ($Ma = 0.75$) is in very good agreement with the experiment

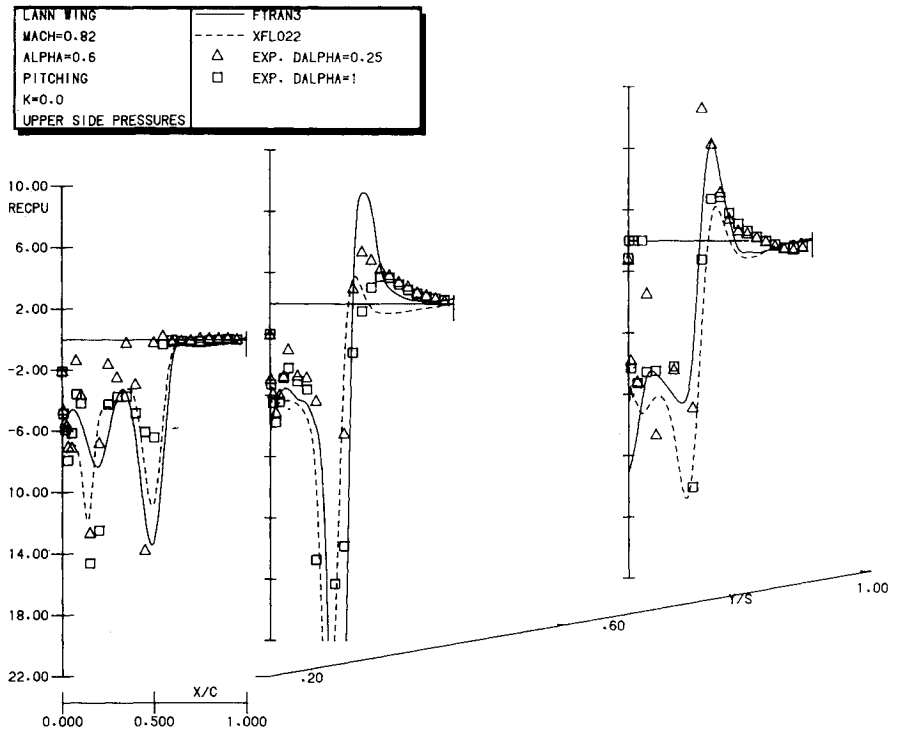

a)

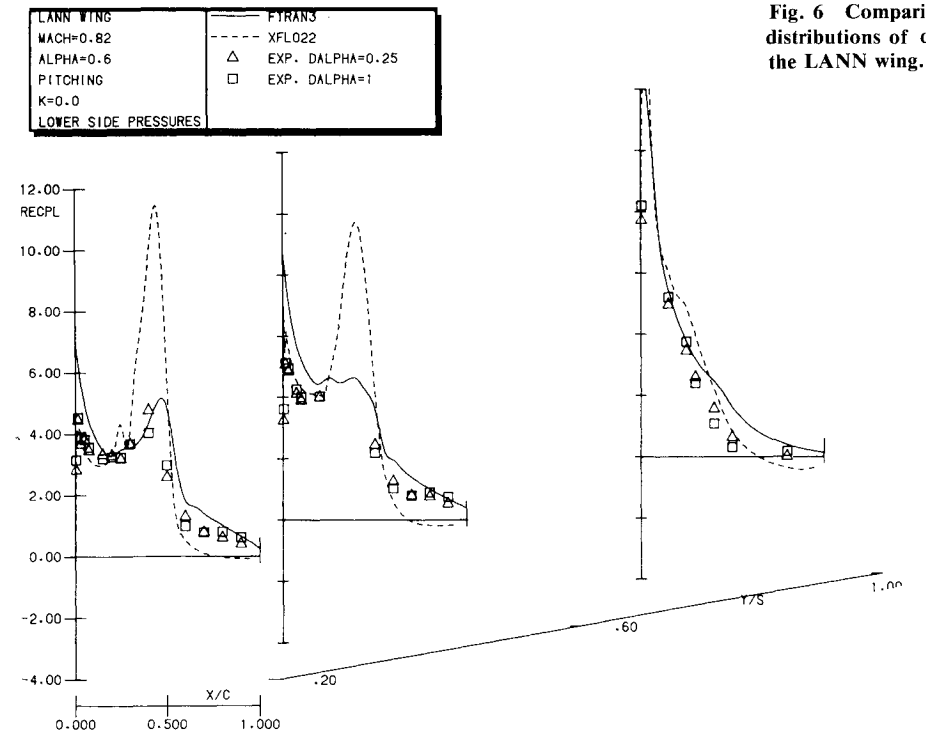

b)

Fig. 6 Comparison of experimental and calculated distributions of quasisteady pressure coefficients on the LANN wing.

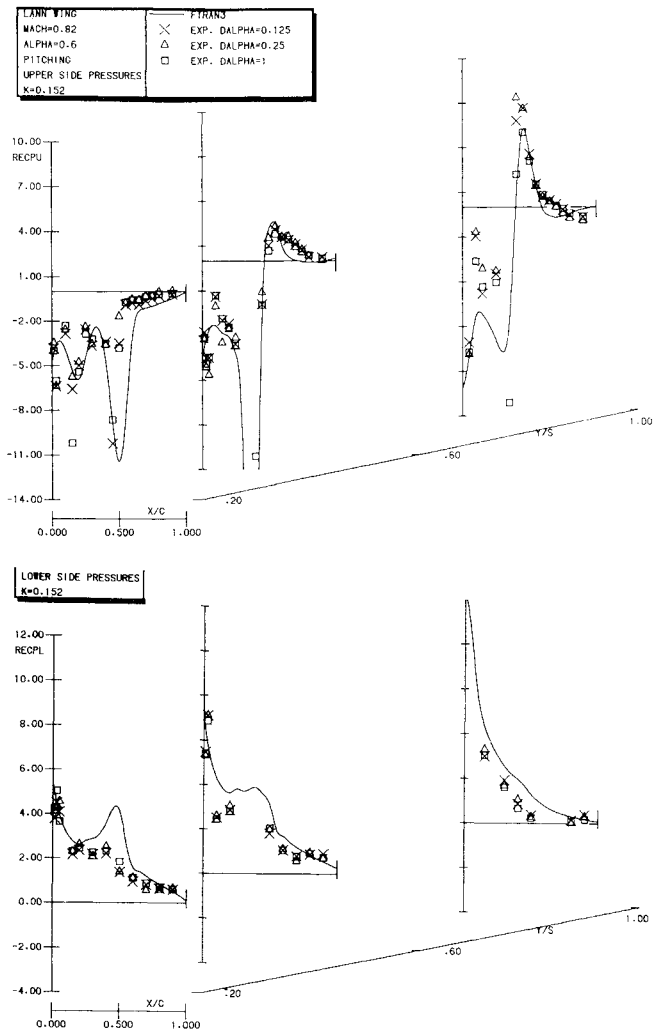

Fig. 7 Comparison of experimental and calculated distributions of the real part of unsteady pressure coefficients on the LANN wing at low reduced frequency.

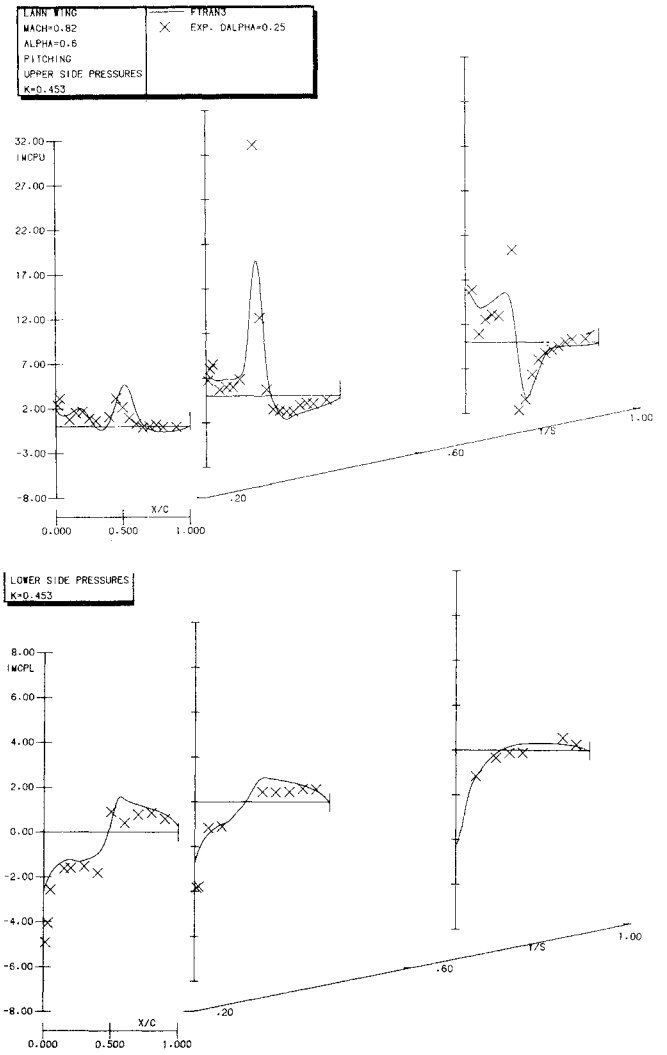

Fig. 8 Comparison of experimental and calculated distributions of imaginary part of unsteady pressure coefficients on the LANN wing at moderate reduced frequency.

and also the effect of the grid is quite small. The second application predicts a nonconservative flutter boundary. The fact that the difference between the coarse and fine-grid results is large compared with the former case indicates a higher sensitivity for an accurate description of the steady and/or unsteady flowfield. The unsteady pressure distribution at the tip, upper side, already presented in Fig. 13, may confirm this in view of the large spanwise gradients at the shock peak. Adding to this that the vibration modes measured during a vibration test at zero speed are less accurate especially in the tip region, the flutter result may have been influenced in a nonconservative sense. It is obvious that more flutter calculations are necessary to present a better weighed judgment.

Fighter-type Configuration

The potential use of FTRAN3 in flutter analyses is further demonstrated for a modern fighter-type configuration in transonic flow. To emphasize the transonic effects on the wing, only the clean wing configuration has been studied at $Ma = 0.9$ and $\alpha = 1$ deg. Within the scope of exemplifying the FTRAN3 method, the maximum frequency of the vibration modes considered has been restricted to 15 Hz.

Steady Flowfield

The fighter configuration is shown in Fig. 15. In this case the body influence is simulated with the NLR panel method by calculating velocities in a cross-wind plane outside the strake. XFLO22 runs, without accounting for aeroelastic deformation, were performed for $Ma = 0.9$ and $\alpha = 1$ deg. Figure 16 shows a comparison of calculated and experimental pressure coefficients at selected stations along the span. The experimental pressure coefficients have been obtained by interpolation between wind tunnel test data. Even for this highly tapered wing the good agreement at the inboard station demonstrates a proper simulation of the fighter fuselage effect on the wing by XFLO22. Near the tip the agreement is less, probably due to less grid resolution in this area.

Unsteady Airloads

Unsteady airloads have been obtained with the NLR doublet-lattice method and FTRAN3.

Doublet-lattice Airloads

The unsteady airloads involve effects of the tip launcher, strake, fighter body, and tail (Fig. 17a) for reduced frequencies based on the full span up to $k = 11.7$. As an example, the antisymmetric vibration modes were calculated up to 15 Hz using the structural representation shown in Fig. 17b, and approximated with a surface spline technique[10] using appropriate conditions at the flap edges. In Fig. 17c, the first two structural vibration modes are shown.

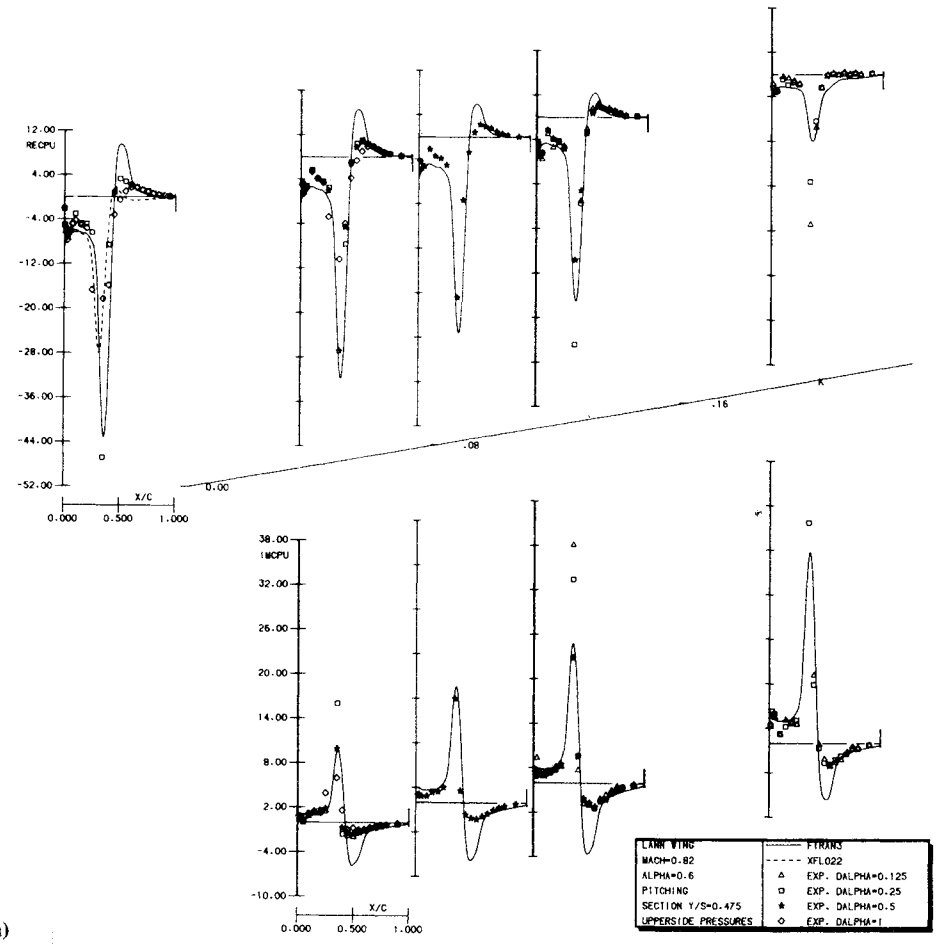

a)

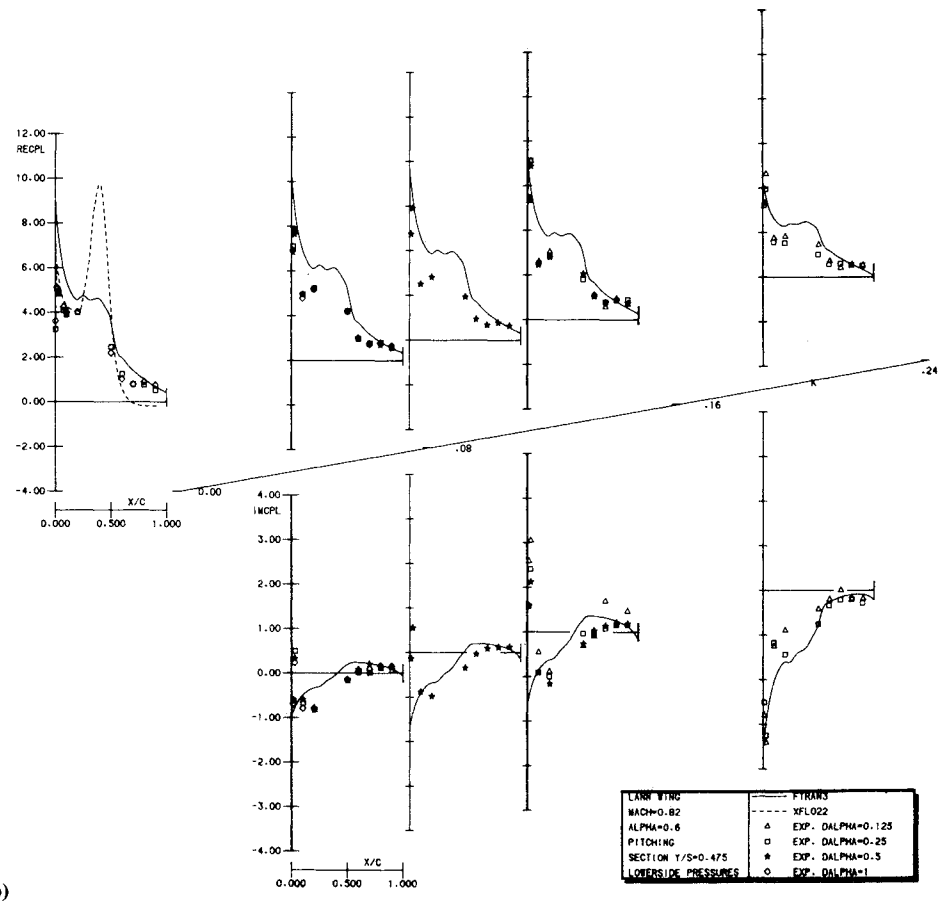

b)

Fig. 9 Comparison of experimental and calculated frequency-wise distributions of unsteady pressure coefficients on the LANN wing at section $Y/S = 0.475$.

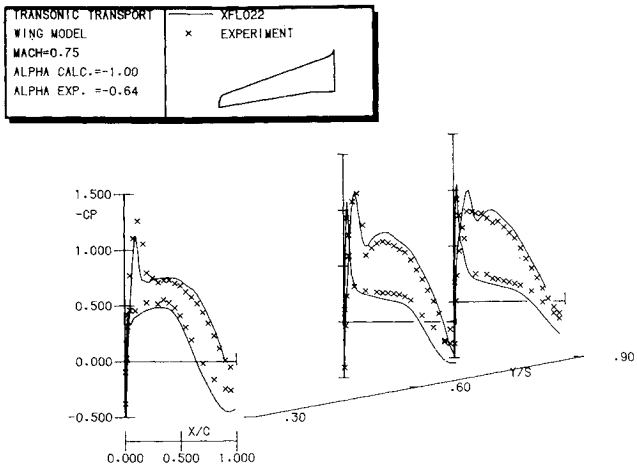

Fig. 10 Comparison of experimental and calculated distributions of steady pressure coefficients on a transonic transport wing model at $Ma = 0.75$.

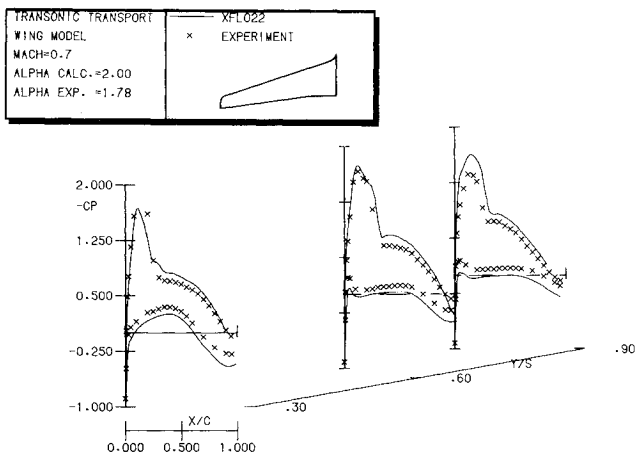

Fig. 11 Comparison of experimental and calculated distributions of steady pressure coefficients on a transonic transport wing model at $Ma = 0.70$.

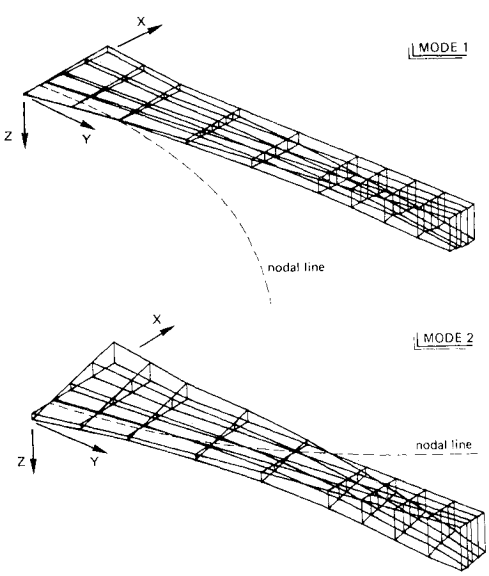

Fig. 12 Vibration modes of a transonic transport wing model.

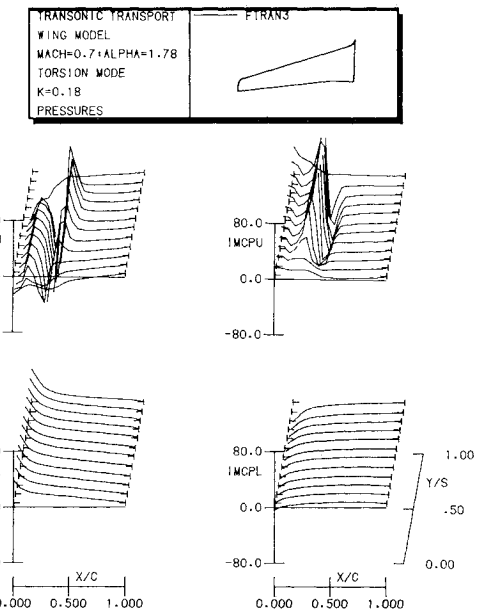

Fig. 13 Calculated distributions of unsteady pressure coefficients on a transonic transport wing model in torsion mode.

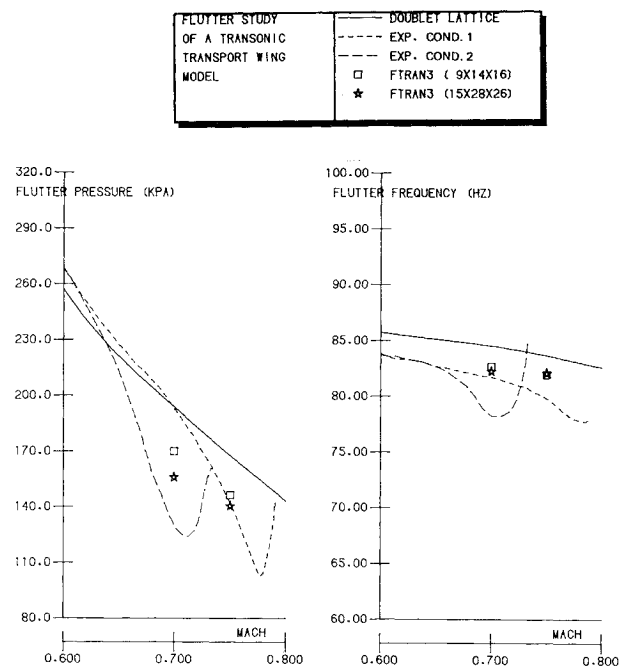

Fig. 14 Flutter results according to doublet lattice, experiment, and FTRAN3.

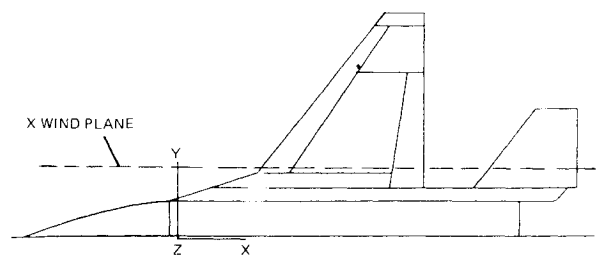

Fig. 15 Fighter configuration.

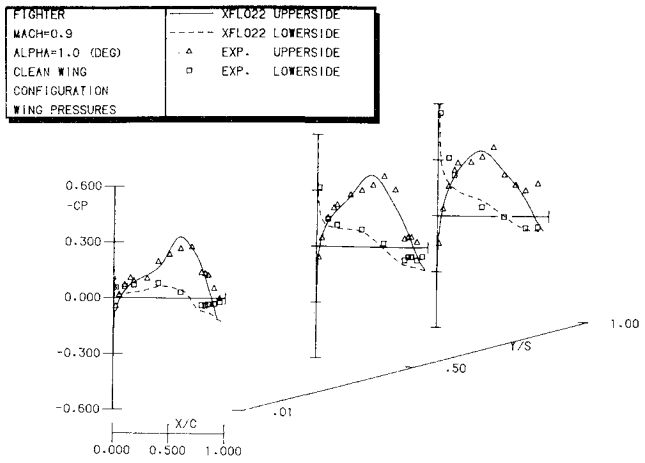

Fig. 16 Comparison of experimental and calculated distributions of steady pressure coefficients on fighter wing.

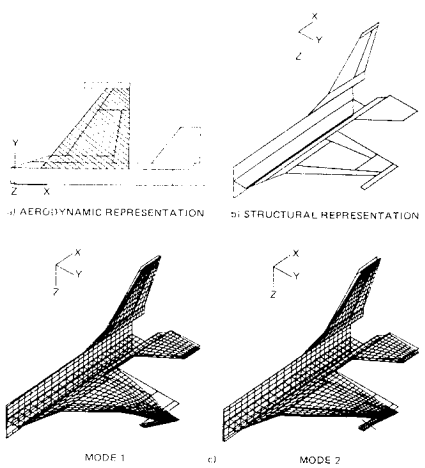

Fig. 17 Aerodynamic and structural modeling of fighter configuration.

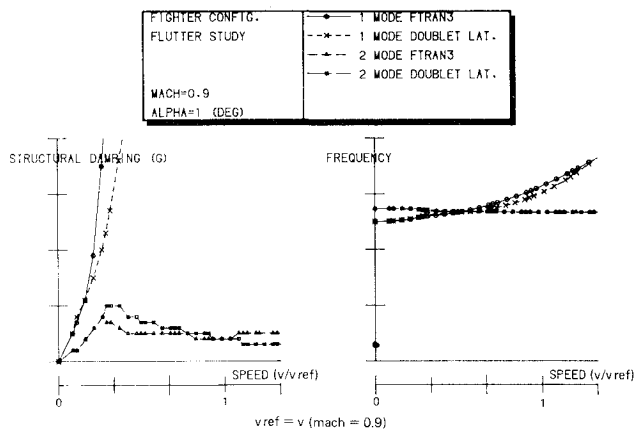

Fig. 18 Flutter characteristics of fighter configuration.

FTRAN3 Airloads

The FTRAN3 code has been applied for the wing part only, as indicated by the shadowed area in Fig. 17a; for the rigid roll mode and the first two vibration modes (Fig. 17c); for five reduced frequencies up to $k=3.4$, based on full span; and for $Ma=0.9$, where transonic effects are significant. Unsteady airloads have been obtained for the whole configuration by replacing the wing contribution of the doublet-lattice airloads by FTRAN3 airloads. At higher reduced frequencies, $k>3.4$, the results of FTRAN3 were nearly equal to those of the doublet-lattice method so that this method has been applied straightforwardly for these cases.

Flutter Characteristics

Preliminary flutter calculations for the fighter-type configuration have been performed with the k method. Figure 18 shows a flutter diagram of the first two vibration modes for $Ma=0.9$ and $\alpha=1$ deg. Up to $v=v_{ref}$ the transonic airloads have a decreasing effect on the stability as compared with the subsonic airloads. Starting at $v=v_{ref}$ the stability increases using transonic airloads.

Conclusions

Application of FTRAN3 and XFLO22 to two transport-type wings and a fighter configuration leads to the following conclusions:

1) Quasisteady results of FTRAN3 and XFLO22 calculations correlate reasonably well.

2) Steady and quasisteady results of calculations with XFLO22 show a reasonable agreement with experimental data.

3) Fighter fuselage effects on steady wing pressures are simulated successfully using the XFLO22 code.

4) Unsteady results of FTRAN3 calculations show a reasonable agreement with experimental data.

5) Application of FTRAN3 in flutter calculations has shown the influence of transonic effects.

However, further analysis and more results are needed to present a more complete picture of this influence.

Acknowledgment

This investigation has been carried out partly under contract with the Scientific Research Division of the Directorate of Materiel, Royal Netherlands Air Force.

References

[1]Isogai, K., "Numerical Simulation of Transonic Flutter of a High-Aspect-Ratio Wing," NAL TR-776T, 1983.

[2]Hounjet, M. H. L., "A Hybrid Field Panel/Finite Difference Method for 3-D Potential Unsteady Transonic Flow Calculations," AIAA Paper 83-1690, July 1983.

[3]van der Vooren, J., van der Kolk, J. Th., and Slooff, J. W., "A System for the Numerical Simulation of Sub- and Transonic Flow Around Wing-Body Configurations," AIAA Paper 82-0935, June 1982.

[4]Labrujere, Th. E., Loeve, W., and Slooff, J. W., "An Approximate Method for the Calculation of the Pressure Distribution on Wing-Body Combinations at Subcritical Speeds," AGARD CP 71, Paper 11, 1970; also, NLR MP 70014 U, 1970.

[5]Hassig, H. J., "An Approximate True Damping Solution of the Flutter Equation by Determinant Iteration," *Journal of Aircraft*, Vol. 7, Nov. 1971, pp. 885-889.

[6]Horsten, J. J., den Boer, R. G., and Zwaan, R. J., "Unsteady Transonic Pressure Measurements on a Semi-span Wind Tunnel Model of a Transport Type Supercritical Wing (LANN model)," NLR TR 82096 U, Pts. 1-3, 1983; also, AFWAL TR-83-3039.

[7]Persoon, A. J., Horsten, J. J., and Meijer, J. J., "On Measuring Transonic Dips in the Flutter Boundaries of a Supercritical Wing in the Wind Tunnel," AIAA Paper 83-1031, May 1983.

[8]Steiginga, A. and Houwink, R., "Correlation of Experimental and Quasi-3D Theoretical Airloads on the Oscillating LANN Supercritical Wing Model," NLR TR 83003 U, 1983; also, AFWAL TR 83-050.

[9]Zwaan, R. J., "Verification of Calculation Methods for Unsteady Airloads in the Prediction of Transonic Flutter," NLR MP 84016 U.

[10]Harder, R. L. and Desmarais, R. N., "Interpolation Using Surface Splines," *Journal of Aircraft*, Vol. 9, Feb. 1972, pp. 189-191.

[11]Jameson, A. and Caughey, D. A., "Numerical Calculations of Transonic Flow Past a Swept Wing," ERDA Rept. COO-3077-140, Courant Institute of Mathematical Sciences, New York University, 1977.